A Study on Wing Structural Design and Sizing for a Large Battery-Electric Aircraft

Wang, Z.; De Breuker, R.; Sodja, J.

DOI
10.2514/6.2025-3470

Publication date
2025

Document Version
Final published version

Published in
AIAA aviation forum and ASCEND 2025

Citation (APA)
Wang, Z., De Breuker, R., & Sodja, J. (2025). A Study on Wing Structural Design and Sizing for a Large Battery-Electric Aircraft. In *AIAA aviation forum and ASCEND 2025* Article AIAA 2025-3470
https://doi.org/10.2514/6.2025-3470

AIAA Aviation Forum and ASCEND co-located Conference Proceedings
21 - 25 July 2025, Las Vegas, Nevada
AIAA AVIATION FORUM AND ASCEND 2025

10.2514/6.2025-3470

A Study on Wing Structural Design and Sizing for a Large Battery-Electric Aircraft

Zhijun Wang*, Roeland De Breuker†, Jurij Sodja‡
Delft University of Technology, Kluyverweg 1, 2629HS Delft, The Netherlands

Rob E. Wolleswinkel§, Reynard de Vries¶, Andrea Giuffré‖
Elysian Aircraft, Rendementsweg 2, 3641SK Mijdrecht, The Netherlands

In the development of large battery-electric aircraft, integrating the batteries into the wing is a crucial decision, as it results in a lighter wing structure due to bending relief. To understand the influence of wing-integrated batteries on wing structures, this paper presents a study on the wing structural design and sizing of the Elysian E9X aircraft configuration. In this study, the baseline wing design is defined, and the critical load cases for wing sizing are identified. Wing structural sizing is performed using an in-house aeroelastic optimization tool. The objective of the optimization is to minimize wing mass by adjusting the thickness of the wing design sections, subject to various design constraints, including structural strength, buckling, and aeroelastic instability. Sensitivity studies on wing mass with respect to key design parameters are conducted. The study results confirm that placing the batteries in the wing results in a significant wing structural mass reduction compared to housing the batteries in the fuselage. The wing mass sensitivities to other design parameters, such as the spanwise position of the main landing gear, may serve as input for the next round of aircraft design.

I. Nomenclature

Variables

n = Load factor [-]
V_C = Cruise speed [m/s]
V_D = Dive speed [m/s]
L = Lift [N]
W_L = Maximum landing weight [N]
m_{s3} = Mass of wing skins, spars, and stringers [kg]
m_{ribs} = Mass of wing ribs [kg]
m_{wb} = Mass of wingbox [kg]
m = Total wing mass [kg]
m_0 = Total mass of the baseline wing [kg]
t/c = Airfoil thickness-to-chord ratio [-]

List of Abbreviations

ASM = Aerospace Structures and Materials
FEM = Finite Element Model

---

*Postdoctoral researcher, Faculty of Aerospace Engineering, z.wang-16@tudelft.nl.
†Professor, Faculty of Aerospace Engineering, R.DeBreuker@tudelft.nl, AIAA Associate Fellow.
‡Assistant Professor, Faculty of Aerospace Engineering, J.Sodja@tudelft.nl, AIAA Senior Member.
§Co-CEO and CTO, rob@elysianaircraft.com, AIAA Senior Member.
¶Chief Engineer, reynard@elysianaircraft.com, AIAA Senior Member.
‖Senior Thermal Engineer, andrea@elysianaircraft.com, AIAA member.

VLM = Vortex Lattice Method
GCMMA = Globally Convergent Method of Moving Asymptotes
EAS = Equivalent Airspeed
SL = Sea Level
LPs = Lamination Parameters
MTOM = Maximum Take-off Mass
MLG = Main Landing Gear
CFD = Computational Fluid Dynamics
CFRP = Carbon Fiber Reinforced Polymer

II. Introduction

Electric aircraft have been recognized as one of the most promising solutions towards climate-neutral aviation. To date, there has been significant research and development on electric aircraft technologies in both academia and industry. In general, many existing studies conclude that battery-electric aircraft are suitable only for small payloads and short ranges due to the limitations of battery technology [1–3].

This, however, has been challenged by recent studies conducted by Elysian Aircraft [4, 5], which demonstrate that developing large battery-powered electric aircraft (e.g., with 90 passengers) is both feasible and meaningful, given the appropriate selection of top-level aircraft requirements and design choices.

To further verify the technical feasibility of the large battery-electric aircraft at the subsystem level, ten *Challenges* have been identified for further research [5]. One of the key research and design tasks, based on these *Challenges*, is to perform wing structural sizing for aeroelastic and landing loads with batteries integrated into the wing (*Challenge 2*). Placing batteries in the wing not only utilizes the wing space but also contributes to wing weight reduction due to the decrease in wing root bending moment (bending relief).

In order to further understand the effect of batteries on the wing structural design of large battery-electric aircraft, this study investigates the preliminary structural design and sizing of the Elysian E9X aircraft wing using an aeroelastic optimization tool. Additionally, sensitivity studies on wing weight with respect to key design parameters are conducted, which may serve as input for the next round of aircraft design.

III. Aeroelastic Optimization

A. Optimization Tool

In the current work, wing structural sizing is realized using an aeroelastic optimization tool named PROTEUS. PROTEUS is an in-house tool developed within the ASM group at Delft University of Technology, and it has been validated and applied to various design cases in both academia and industry [6–10].

In PROTEUS, wing structures (i.e., skins and spars) are divided into a series of design sections, so that the stiffness properties of each section can be tailored in the desired directions. In this way, PROTEUS is often employed to explore the potential of passive load alleviation through aeroelastic tailoring of composite wings.

For structural analysis, the 3D wing is modeled as a clamped beam using a geometrically nonlinear beam Finite Element Model (FEM), where the properties of each beam element are determined via a cross-sectional modeler [11]. The aerodynamic response of the wing is predicted using an unsteady Vortex Lattice Method (VLM) based on potential flow theory [12]. Accordingly, the static aeroelastic model of the wing is built by coupling the beam FEM and the unsteady aerodynamic model, which is solved using the Newton-Raphson root-finding method. The gradient-based optimizer, Globally Convergent Method of Moving Asymptotes (GCMMA) [13], is employed in PROTEUS to update design variables with analytic sensitivities. Further details on PROTEUS can be found in the work of Werter and De Breuker [6] and references therein.

It is worth noting that PROTEUS is capable of considering both manoeuvre and gust loads for wing structural sizing, but gust loads are not included in the current study. Examples of wing sizing with PROTEUS that include gust loads can be found in the work of Wang et al. [8], Rajpal et al. [14].

B. Optimization Model

Within the PROTEUS framework, the optimization *objective* in this work is to minimize the wing structural mass. Note that the objective function in PROTEUS is not limited to mass minimization; it can also include objectives such as range maximization or tip displacement minimization.

The *design variables* include the thickness of each wing design section and, in cases where composite materials are used, the Lamination Parameters (LPs) of the wing laminates. Additionally, the wing jig (unloaded) twist angles, defined within the PROTEUS beam FEM framework, are included as design variables to maintain the desired wing cruise shape during optimization. Further details on the wing jig twist design variables and the cruise shape constraint can be found in the work of Wang et al. [8], Sodja et al. [15].

To ensure the feasibility of the wing design, various aerostructural design *constraints*, as described in Table 1, are included in the aeroelastic optimization. The modeling and numerical implementation of these design constraints are detailed in the work of Werter and De Breuker [6], Wang et al. [8] and references therein. Note that lamination feasibility constraints are included only when composite materials are used for wing structural sizing.

Table 1 Design constraints considered in the aeroelastic optimization.

Constraint	Description
Lamination feasibility	To ensure the LPs represent a feasible laminate
Structural strength	A strain factor defined to indicate strength failure
Buckling load	A buckling factor defined to indicate buckling stability
Aeroelastic stability	Flutter is governed by the real parts of the eigenvalues of the state matrix
Aileron effectiveness	To ensure aileron performance
Local angle of attack	To ensure attached aerodynamic flow
Cruise (1 g) shape	To maintain the desired target twist distribution during cruise

IV. Baseline Wing Design

A. Baseline Wing Model

To design the baseline wing and generate its PROTEUS inputs for structural sizing, the flowchart illustrated in Fig. 1 is followed, since the definition of one component (e.g., a rib) is highly dependent on other wing components (e.g., control surfaces).

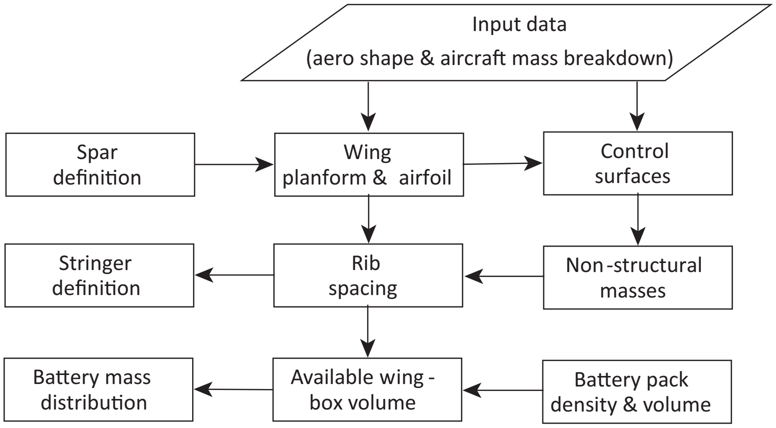

Fig. 1 Flowchart for defining the baseline wing.

Fig. 2 depicts the wing structural model generated by PROTEUS, where the Main Landing Gear (MLG), batteries, electric engines, and rotors are modeled as non-structural masses. In particular, the battery mass distribution is determined based on the available volume of the wingbox sections between each pair of adjacent ribs. The main characteristics of the baseline wing are listed in Table 2, and an isotropic material (i.e., aluminum alloy 2024-T3) is used for the wing skins, spars, ribs, and stringers. As shown in Table 2, the mass of batteries installed in the wing accounts for nearly half (46%) of the aircraft's Maximum Take-off Mass (MTOM).

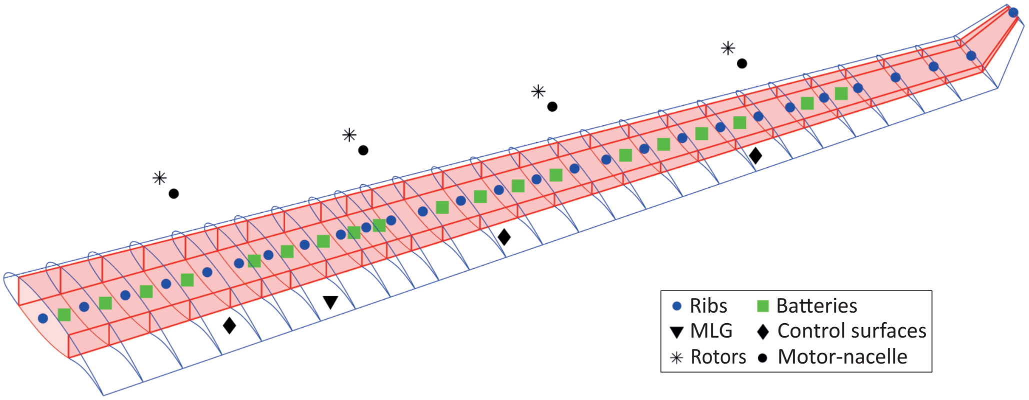

Fig. 2 Structural analysis model of the baseline wing (generated using the PROTEUS tool).

Table 2 Main characteristics of the baseline wing.

Wing span [m]	Aspect ratio [-]	Planform area [m^2]	Root chord [m]	Tip chord [m]	MTOM [kg]	Battery mass [kg]
42	12	148	5	2	76,000	35,000

B. Critical Load Cases

To size the wing structures in PROTEUS, critical load cases must be identified and provided as input. To this end, the V-n diagram of the E9X aircraft is drawn in accordance with CS-25 [16]. Fig. 3 illustrates the aircraft's V-n diagram, including both the manoeuvre and gust envelopes.

According to the V-n diagram, Table 3 lists the critical load cases considered in the preliminary wing structural sizing. *Load Case 1* represents the cruise flight condition, which is included mainly to implement a cruise (1 g) shape constraint in order to ensure the desired cruise aerodynamic performance. *Load Cases 2* and *3* correspond to 2.5 g symmetric pull-up and -1 g symmetric push-down flight conditions, respectively. *Load Case 4* has the same load factor as *Load Case 2*, and this load case is considered as the equivalent gust load case at sea level. Note that the maximum gust load factor calculated by the Pratt equation [17] is 2.37, and the gust envelope lies within the manoeuvre envelope, as shown in Fig. 3. *Load Case 5* represents the flap-deflected condition at sea level.

Table 3 Identified load cases for wing structural sizing.

ID	Mach number	EAS [m/s]	Altitude [m]	Load factor	Description
1	0.65	133.76	7,620	1	Cruise
2	0.70	167.20	5,618	2.5	Max n at V_D (D-point in Fig. 3)
3	0.65	133.76	7,620	-1	Min n at V_C (F-point in Fig. 3)
4	0.40	133.76	0	2.5	Max n at V_C (SL)
5	0.24	81.08	0	2	Max n for flap deflected (SL)
6	0.17	57.33	0	-1.35	Equivalent landing load

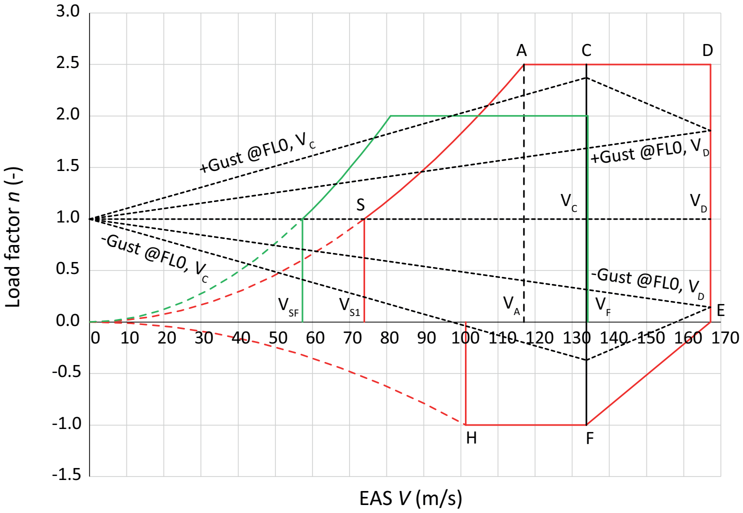

Fig. 3 Aircraft V-n diagram.

Additionally, *Load Case 6* refers to the equivalent landing load, and it is included to account for the effect of landing load on wing structural sizing within the PROTEUS framework. The equivalent load factor is calculated by assuming a two-point level landing with $L = W_L$. The kinetic energy of the aircraft during landing is absorbed by the MLG shock absorber, and the work done by the shock absorber is related to its nominal stroke length. In addition to including *Load Case 6* for consideration of the landing load, a point force, calculated based on the work done by the shock absorber, is applied at the MLG location in the wing structural model.

C. Wing Structural Sizing

The wing structural sizing aims to minimize wing mass by optimizing the thickness of the design sections, subject to various design constraints. The aeroelastic optimization setup for wing sizing is listed in Table 4. Note that, since an isotropic material is used for the baseline wing, no design variables related to LPs and lamination feasibility constraints are included in this optimization. However, they are included in the composite wing sizing presented in Section V.C.

Table 4 Wing aeroelastic optimization setup.

Type	Parameter	# variables
Objective	Minimize wing mass	1
Design variables	Wing section thickness	72
	Twist angle (wing jig shape)	23
	Wing section LPs*	$72 \times 8 = 576$
Constraints	Lamination feasibility*	$72 \times 6 = 432$
	Static strength	1,104 per load case
	Buckling	4,608 per load case
	Aeroelastic stability (e.g., flutter)	10 per load case
	Aileron effectiveness	1 per load case
	Local angle of attack	50 per load case
	1 g twist angle distribution	48
	Total number of constraints (6 load cases)	34,686 (or 35,118*)

* *Only applicable for the composite wing.*

Fig. 4 shows the optimized thickness distribution of the wing skins and spars. Overall, the wing thickness decreases from the root to the tip, corresponding to the maximum bending and torsional moments at the wing root. In the inboard portion of the top skin, the leading-edge sections are tailored to be thicker than their counterparts, resulting in a forward shift of the elastic axis. This introduces wash-out (nose-down) twist during wing bending, which shifts aerodynamic load inboard and, consequently, reduces wing mass by lowering the wing root bending moment.

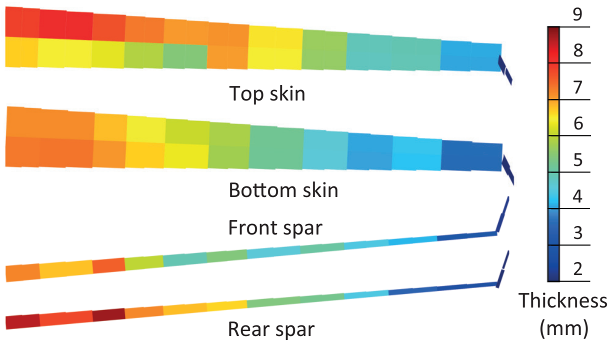

Fig. 4 Optimized thickness distribution of wing skins and spars.

To further understand which load cases and design constraints govern the wing sizing, Figs. 5 and 6 illustrate the distributions of the critical strain and buckling factor, where the critical value is defined as the maximum strain or buckling factor among the six load cases. Note that, by definition, the maximum strain and buckling factors are equal to one, but they are 0.67 here due to the incorporation of a safety factor of 1.5 (whereas 0.7 is used in the legends of Figs. 5 and 6 for plotting purposes only).

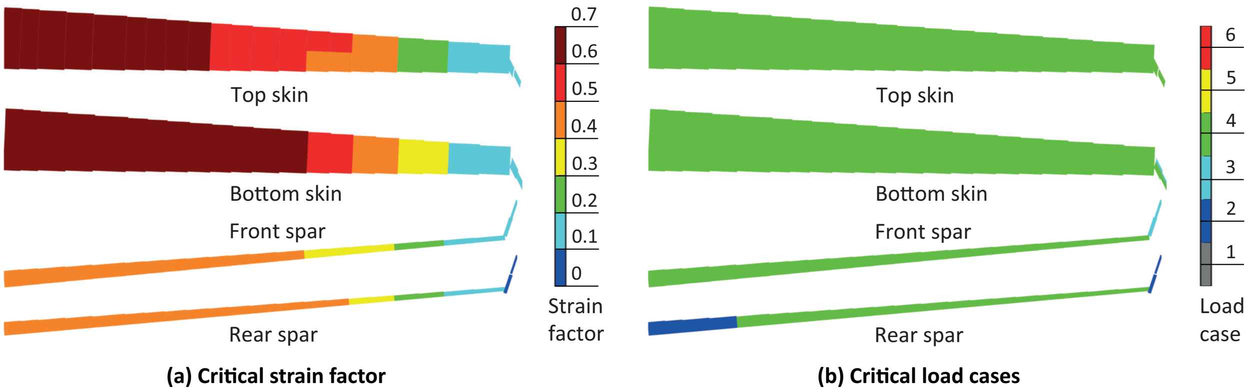

(a) Critical strain factor

(b) Critical load cases

Fig. 5 Distributions of (a) the critical strain factor and (b) the sizing load cases for the aluminum wing.

As can be observed in Fig. 5(a), the inner portion of the wing skins is mainly sized by structural strength, while buckling constraints are primarily active at the wing spars and the outer portion of the wing skins, as shown in Fig. 6(a). Furthermore, as shown in Fig. 5(b), *Load Case 4* is critical for the structural strength of both the skins and spars, as well as for the buckling of the wing top skin, since it represents the equivalent gust load with the maximum load factor is considered at sea level. As can be seen in Fig. 6(b), the buckling constraints of the bottom skin are active under *Load Case 3* due to the negative load factor.

D. Wing Mass Estimation

In PROTEUS, only the weight of the wingbox can be estimated based on the beam FEM. The total wing mass can be predicted using an empirical correlation formulated as

$$m = 1.74 m_{wb} = 1.74 \times (m_{s3} + m_{ribs}), \tag{1}$$

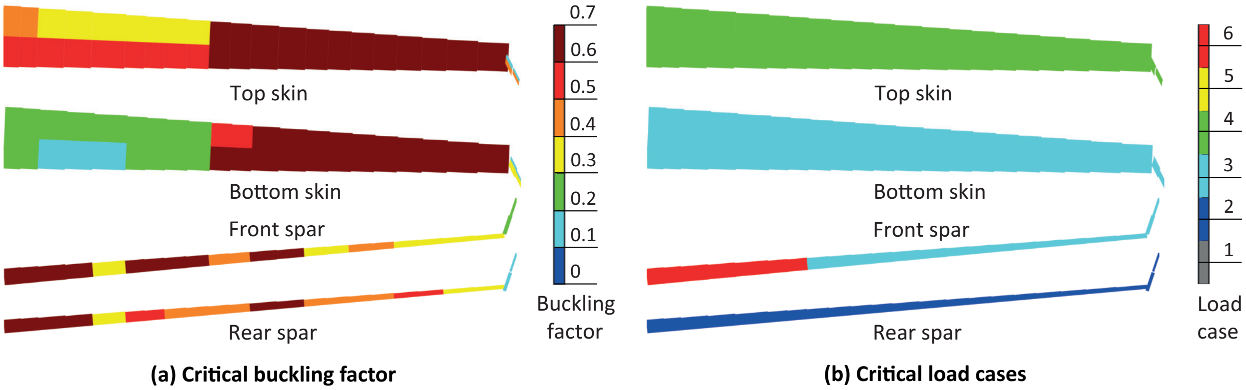

Fig. 6 Distributions of (a) the critical buckling factor and (b) the sizing load cases for the aluminum wing.

where the total wing mass m is obtained by scaling the wingbox mass m_{wb} using a factor of 1.74, according to the work of Ardema et al. [18]. The wingbox mass includes the mass of the wing skins, spars, and stringers (denoted as m_{s3}), which is the variable optimized by PROTEUS. The mass of the ribs, m_{ribs}, is treated as a constant value estimated based on the wing section area and rib material properties.

It is worth noting that the mass estimated for the baseline wing serves as a reference for investigating mass variation in the sensitivity studies (presented in Section V), and that the current work does not aim to obtain a practical estimate of the total wing mass. Accordingly, a parameter δ, defined as

$$\delta = (m - m_0)/m_0 \times 100\% \,, \tag{2}$$

is used to quantify the mass difference relative to the baseline wing mass m_0.

V. Sensitivity Studies

To understand the effects of wing-integrated batteries and structural design on wing structural weight, several sensitivity studies are conducted on key design parameters, such as battery location, the spanwise position of the MLG, and the number and location of spars.

A. Battery Location

In the baseline wing design, the batteries are placed within the wingbox. To quantify the mass reduction resulting from integrating batteries into the wing, the baseline wing is resized with the batteries relocated to the fuselage.

Fig. 7 shows the optimized thickness distribution of the wing with batteries placed in the fuselage, as well as the thickness differences between the optimized wings with batteries located in the wingbox and in the fuselage. It is clear that placing the batteries in the fuselage increases the thickness of the top and bottom skins, as well as parts of the spars.

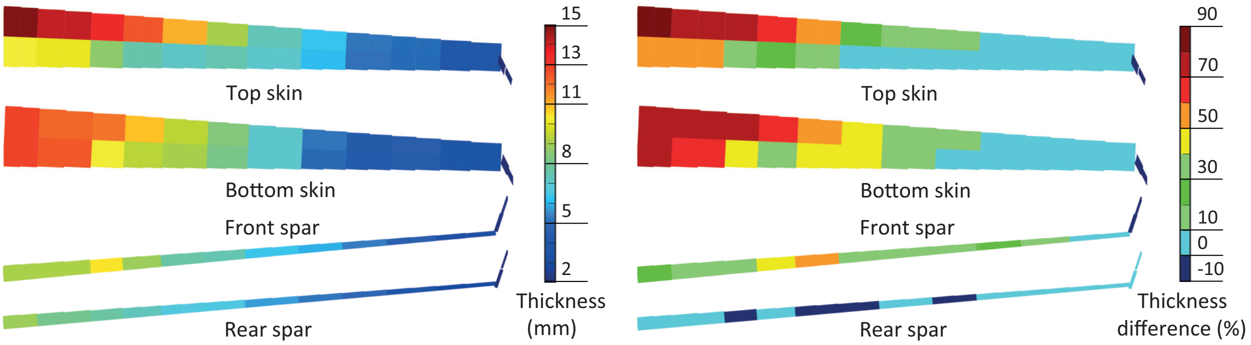

Fig. 7 Optimized thickness distribution of the wing with the battery placed in the fuselage (left) and the thickness differences compared to the baseline wing (right).

According to the current study, placing the batteries in the fuselage increases wing structural weight by approximately 32% compared to integrating the batteries into the wing (i.e., $\delta = 32\%$). It is also worth mentioning that placing the batteries in the fuselage could lead to an even heavier wing structure when considering the snowball effect of fuselage resizing, along with the additional structural weight required to accommodate the battery volume in the fuselage.

B. MLG Spanwise Position

To investigate the influence of the MLG spanwise position (i.e., y-coordinate) on wing structural weight, the baseline wing is resized for seven different spanwise positions, with $y = 5.78$ m taken as the reference, as defined in the baseline configuration. It is worth noting that $y = 5.5$ m and $y = 6.23$ m correspond to the reference MLG positions of the Boeing 747 and Airbus A380, respectively. Additionally, $y = 3.98$ m represents one of the spanwise positions of the electric propulsion units.

Fig. 8 illustrates the variation in wing mass with changes in the MLG spanwise position. As observed, there is an optimal spanwise position for the MLG that minimizes wing mass, which is $y = 5.5$ m in the current study. This results from a balance between the upward impact force from the MLG and the downward inertial force during landing.

As shown in Fig. 8, the wing mass difference, δ, ranges from -0.3% to 3%. The effect of the MLG spanwise position on wing mass is relatively small (within ±1%) when the MLG is placed relatively inboard. This is because the wing structure is primarily sized by *Load Case 4* (as shown in Figs. 5 and 6), meaning that the landing load case (*Load Case 6*) has a relatively minor influence on wing mass. However, when the MLG is moved further outboard, the impact becomes more pronounced due to the larger root bending moment generated by the MLG impact force. Additionally, it is important to note that the current analysis considers only the landing load and does not account for taxi bump loads, which may be critical in some cases depending on the shock absorber design.

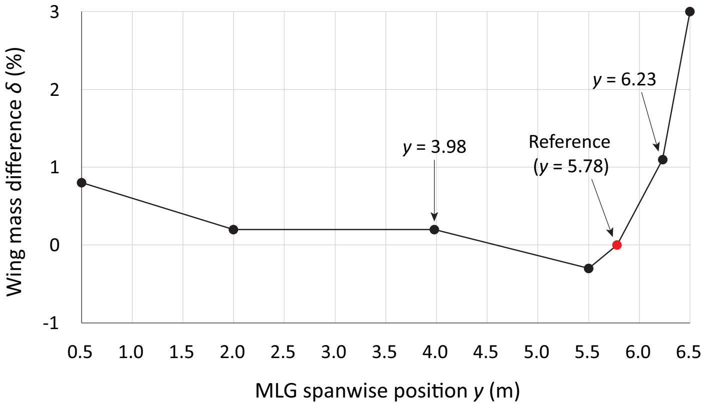

Fig. 8 Wing mass variation with changes in the MLG spanwise position.

C. Material Properties

In this section, both isotropic and anisotropic materials are tested for the design of wing structures. Table 5 lists the material properties used in this sensitivity study. Note that the yield strength is used for aluminum materials to ensure a more conservative design, and the tensile and compressive strengths of isotropic materials (i.e., aluminum alloys) are assumed to be the same.

To investigate the effect of material properties on wing mass, four design cases are defined and listed in Table 6. *Design 1* represents the baseline wing, in which aluminum alloy 2024-T3 is used for both the wing skins and spars, as described in Section IV.A. In *Design 2*, aluminum alloy 7075-T6 is used for the top skin due to its higher tensile and shear strength. In *Design 3*, both the wing skins and spars are made of aluminum alloy 7075-T6. In *Design 4*, the Carbon Fiber Reinforced Polymer (CFRP) composite AS4/3501-6 is used for both the wing skins and spars.

In Table 6, the mass difference δ is provided for *Designs 2-4* relative to the baseline wing (*Design 1*). It can be seen that replacing the top wing skin (*Design 2*) or both the skins and spars (*Design 3*) reduces wing mass, although the reductions are relatively small (less than 1%). In contrast, a significant mass reduction of approximately 22% is achieved when the wing is sized using composite material (*Design 4*).

Table 5 Isotropic and anisotropic material properties.

Material	Aluminum Alloy 2024-T3	Aluminum Alloy 7075-T6	Composite AS4/3501-6
Density ρ [kg/m^3]	2780	2810	1600
Longitudinal elastic modulus E_{11} [GPa]	73.1	71.7	147.0
Transverse elastic modulus E_{22} [GPa]	73.1	71.7	10.3
Shear modulus G_{12} [GPa]	28.0	26.9	7.0
Poisson's ratio ν_{12} [-]	0.33	0.33	0.27
Longitudinal tensile strength X_t [MPa]	345	503	948.5*
Longitudinal compressive strength X_c [MPa]	345	503	717.6*
Transverse tensile strength Y_t [MPa]	345	503	23.7*
Transverse compressive strength Y_c [MPa]	345	503	94.8*
Shear strength S [MPa]	283	331	31.6*

** Including knockdown factors for environmental effects (0.8), barely visible impact damage (0.65), and material scatter (0.8) [19].*

Table 6 Four wing designs sized with different materials and their corresponding mass differences.

Design ID	Material used for wing skins and spars	Mass difference δ
1	Aluminum alloy 2024-T3 (baseline wing)	0
2	2024-T3 for bottom skin and spars, 7075-T6 for top skin	-0.5%
3	Aluminum alloy 7075-T6	-0.6%
4	Composite AS4/3501-6	-21.8%

It should be noted that this mass reduction represents a maximum theoretical value, as the design variables for composite wing sizing are the LPs, which must subsequently be retrieved into manufacturable stacking sequences. For examples of retrieving stacking sequences of composites based on LPs and thickness, the reader is referred to the work of Wang et al. [8], Macquart [20]. In general, a mass penalty will be incurred when the optimized LPs and thicknesses are retrieved into discrete stacking sequences, with the magnitude of this penalty largely depending on the allowable freedom in fiber angles, which requires further study to quantify.

Fig. 9 compares the optimized thickness distributions across the four wing designs with different material properties. As observed, using isotropic (i.e., aluminum alloy) and anisotropic (i.e., CFRP composite) materials leads to two distinct types of designs. Specifically, in aluminum wings (i.e., *Designs 1-3*), the spars are thicker than the skins, as shown in Fig. 9(a)-(c), with the rear spar root sections being the thickest.

In contrast, the composite wing (i.e., *Design 4*) features thicker skins than spars, as shown in Fig. 9(d). This is because structural strength governs the sizing of the entire wing, as illustrated in Fig. 10(a), whereas for the aluminum wing, it is active only in the inner portion of the wing skins, as shown in Fig. 5(a). As observed in Fig. 10(b), *Load Cases 2-4* are critical for sizing different sections of the composite wing, whereas only *Load Case 4* is critical for sizing the aluminum wing, as shown in Fig. 5(b).

Based on the critical buckling factors and sizing load cases shown in Figs. 6 and 11, both aluminum and composite wings are sized by the same critical load cases for buckling. However, the buckling constraint is less active in the inner portion of the composite wing than in the aluminum wing.

Although the composite wing skins are thicker than those made of aluminum, the composite wing remains lighter than the aluminum wings due to its lower material density, as shown in Tables 5 and 6. Additionally, it can be observed that the use of higher-strength 7075-T6 aluminum results in thinner wing skins compared to those made of 2024-T3.

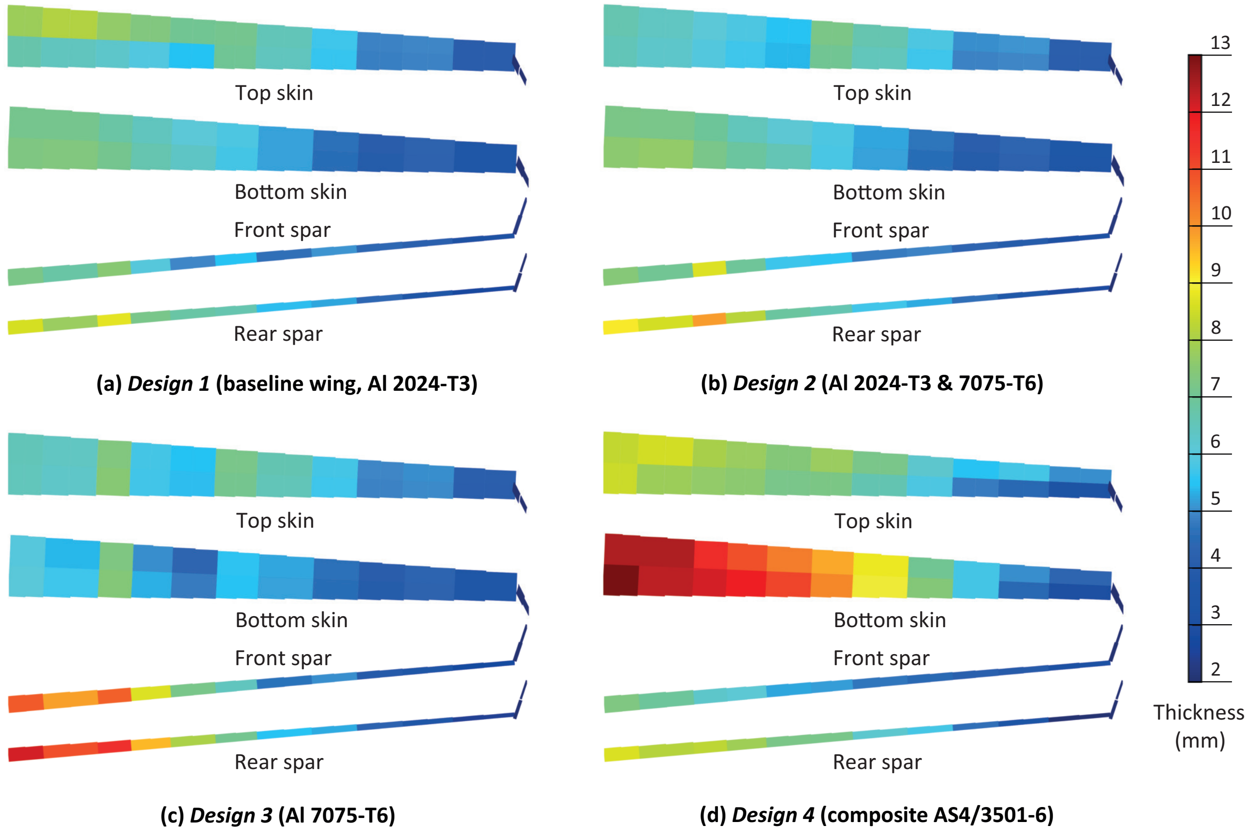

(a) *Design 1* (baseline wing, Al 2024-T3)

(b) *Design 2* (Al 2024-T3 & 7075-T6)

(c) *Design 3* (Al 7075-T6)

(d) *Design 4* (composite AS4/3501-6)

Fig. 9 Optimized thickness distributions of four wing designs sized with different materials.

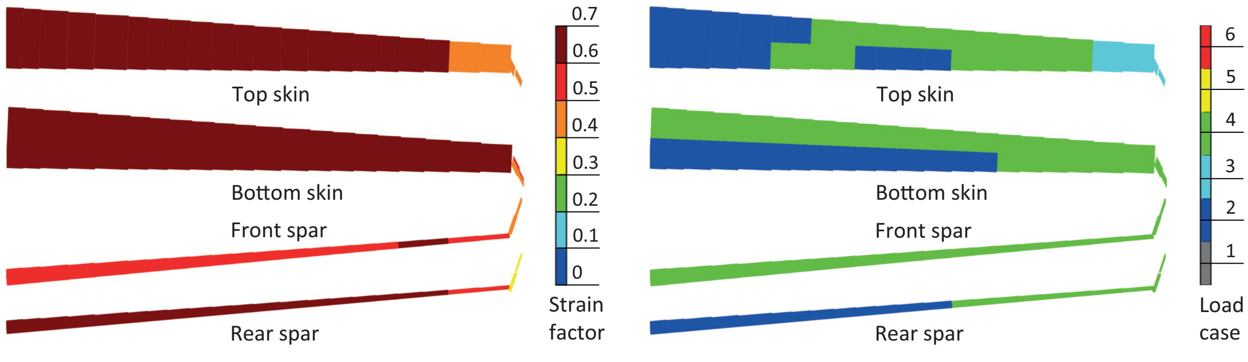

(a) Critical strain factor

(b) Critical load cases

Fig. 10 Distributions of (a) the critical strain factor and (b) the sizing load cases for the composite wing.

D. Thickness-to-Chord Ratio

For the baseline wing, the airfoil types used at the wing root and tip sections are determined based on Computational Fluid Dynamics (CFD) simulations for aerodynamic efficiency, with thickness-to-chord ratios (i.e., t/c) of 17% and 10%, respectively. To quantify the impact of the airfoil t/c on wing mass, the baseline wing is resized by independently varying the t/c of the wing root and tip airfoils. It is worth noting that, with changes in the airfoil t/c, the mass distributions of the batteries and ribs also need to be updated.

Fig. 12 shows the variation in total wing mass (m), mass of ribs (m_{ribs}), and the optimized mass of the wing skins, spars, and stringers (m_{s3}) with changes in the airfoil thickness-to-chord ratio. As expected, the mass of wing ribs increases with an increase in the airfoil t/c, as illustrated by the dashed lines with point markers. However, the

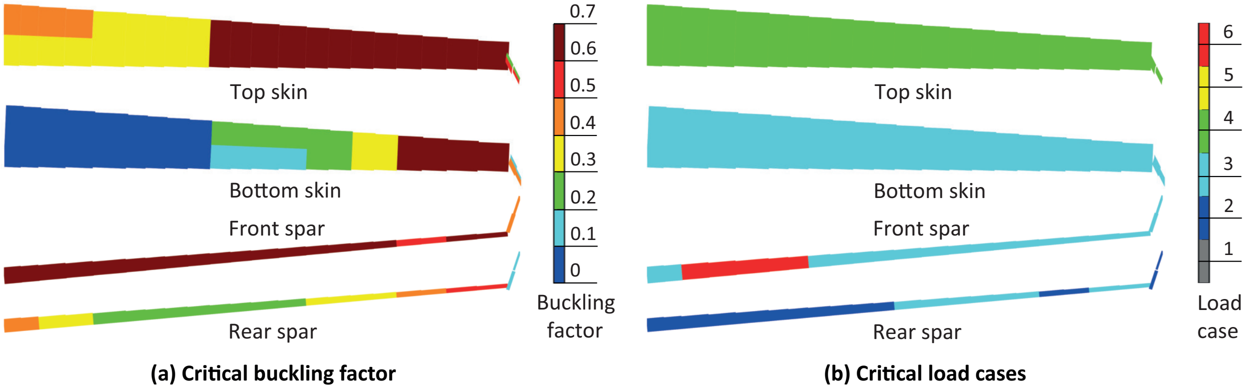

(a) Critical buckling factor (b) Critical load cases

Fig. 11 Distributions of (a) the critical buckling factor and (b) the sizing load cases for the composite wing.

difference in mass of ribs is more pronounced when the wing root airfoil is varied, since the root airfoil ($t/c = 17\%$) is inherently thicker than the tip airfoil ($t/c = 10\%$).

Furthermore, as indicated by the solid lines in Fig. 12, increasing the thickness-to-chord ratio in both the root and tip airfoils leads to a reduction in total wing mass, primarily because thicker airfoils result in a stronger wing structure. Moreover, as illustrated by the dashed lines with triangle markers, increasing the t/c of the wing root airfoil results in greater reduction in the mass of wing skins, spars, and stringers, with maximum mass reductions of approximately 12% and 4% when varying the root and tip airfoils, respectively. This indicates that the root t/c has a more significant impact on wing mass reduction.

On the other hand, the mass reduction in the wing skins, spars, and stringers is offset by an increase in rib mass, leading to a smaller overall reduction in total wing mass. According to the current study, the maximum reduction in total wing mass is approximately 8% ($\delta = -8\%$) when the thickness-to-chord ratio of the wing root increases to 25%.

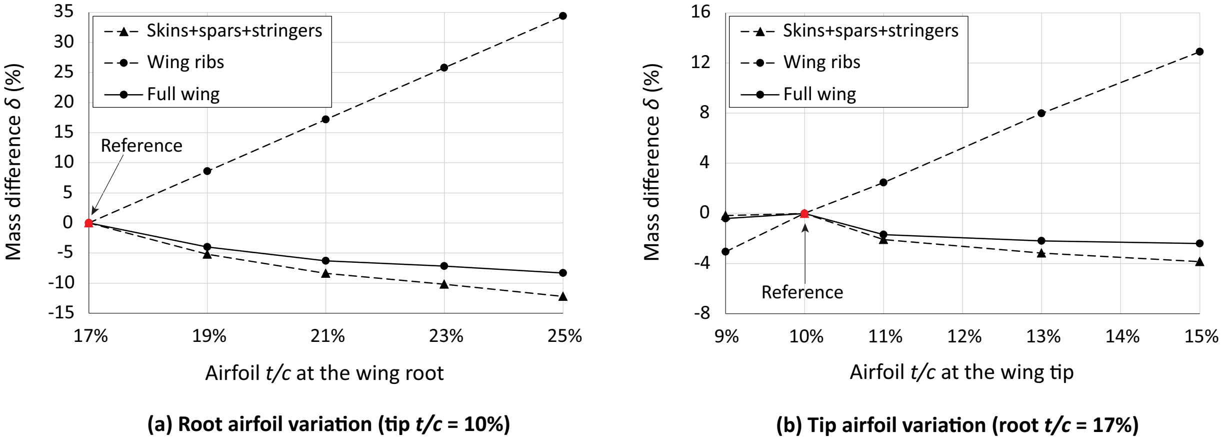

(a) Root airfoil variation (tip *t/c* = 10%) (b) Tip airfoil variation (root *t/c* = 17%)

Fig. 12 Wing mass variation with changes in airfoil thickness-to-chord ratio.

E. Number and Location of Spars

As demonstrated in Section V.A, integrating batteries into the wingbox can substantially reduce wing weight. Accordingly, it is essential to investigate the effects of the number and location of spars on wing mass, as the available wingbox volume is critical for effective battery integration.

In this study, four wingbox configurations, as shown in Fig. 13, are defined and sized. These configurations are generated by combining either two or three spars, with two sets of extreme spanwise spar locations considered.

Fig. 13(a) and Fig. 13(b) depict wide-wingbox *Configurations 1* and *2*, in which the front and rear spars are positioned at 5% and 65% of the wing chord, respectively. It is important to note that, in this study, the extreme front spar location (i.e., at 5% chord) is chosen to maximize the wingbox volume, without accounting for additional structural design considerations, such as bird strike resistance. Fig. 13(c) and Fig. 13(d) illustrate the narrow-wingbox *Configurations 3* and *4*, in which the front and rear spars are positioned at 15% and 55% of the wing chord, respectively. For the 3-spar configurations shown in Fig. 13(b) and Fig. 13(d), the middle spar is positioned at 35% of the wing chord for both wide and narrow wingbox cases.

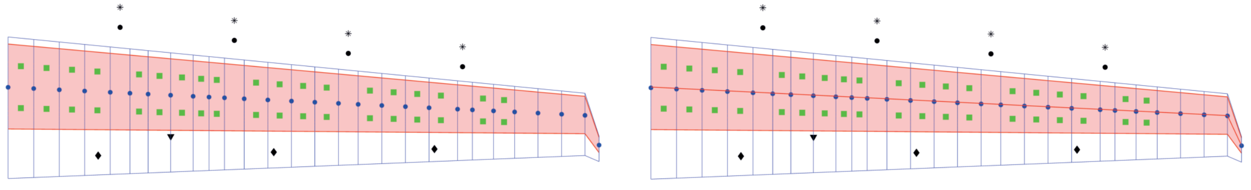

(a) ***Configuration 1***: 2-spar (5% front & 65% rear) (b) ***Configuration 2***: 3-spar (5% front & 65% rear)

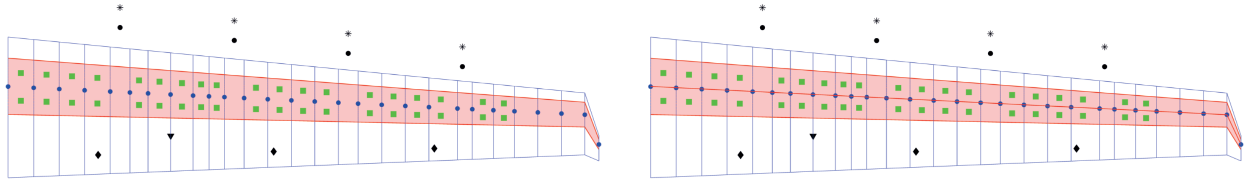

(c) ***Configuration 3***: 2-spar (15% front & 55% rear) (d) ***Configuration 4***: 3-spar (15% front & 55% rear)

● Ribs 🟩 Batteries ▼ MLG ◆ Control surfaces ✳ Rotors ● Motor-nacelle

Fig. 13 Wingbox configurations with different numbers and locations of spars.

In this study, the total number of battery units is assumed to be identical across all four wingbox configurations. However, the battery mass distribution is adjusted for each configuration to account for differences in the available wingbox volume. The remaining definitions and setup parameters for PROTEUS sizing are kept consistent with those defined for the baseline wing.

To enable a fair comparison of total wing mass across different wing configurations, the structural mass of the leading and trailing edges must be included in the total mass estimation. However, since PROTEUS provides only the wingbox mass, a shell FEM is constructed for each configuration in ANSYS Mechanical APDL, using a consistent wing structural model and data exported from PROTEUS. This approach not only allows for a more practical and comprehensive mass estimation, but also provides an opportunity to numerically validate PROTEUS by comparing the structural response obtained from ANSYS and PROTEUS.

Fig. 14 shows the shell FEM of wing *Configuration 1*, as illustrated in Fig. 13(a). Note that the leading and trailing edges are assigned a constant thickness, and the thicknesses of the wing skins and spars exactly match those optimized in PROTEUS. The stringers on the top and bottom wing skins are modeled using beam elements with a rectangular cross-section, since the stringers in PROTEUS are simplified as blade stringers. The loads exported from PROTEUS consist of nodal forces and moments from the wing beam FEM, and they are applied to the ANSYS shell FEM by implementing RBE3-type elements in ANSYS Mechanical APDL.

Table 7 lists the total mass of the wing skins, spars, and stringers (m_{s3}), as well as the mass of ribs (m_{ribs}), estimated by ANSYS and PROTEUS, respectively. The results show that the mass differences between the ANSYS and PROTEUS predictions are relatively small, which verifies the accuracy of the shell FEM in wing mass estimation.

Table 7 Mass comparison of wing structures estimated by ANSYS and PROTEUS (where $\mathbf{m_{s3}}$ denotes the total mass of skins, spars, and stringers, and $\mathbf{m_{ribs}}$ refers to the mass of the ribs).

Configuration	*1*	*2*	*3*	*4*
Number of spars	2-spar	3-spar	2-spar	3-spar
Spar spanwise position (% chord)	5% & 65%	5% & 65%	15% & 55%	15% & 55%
m_{s3} difference (ANSYS vs. PROTEUS)	1.0%	0.6%	0.2%	0.8%
m_{ribs} difference (ANSYS vs. PROTEUS)	-1.6%	-1.6%	-1.5%	-1.5%

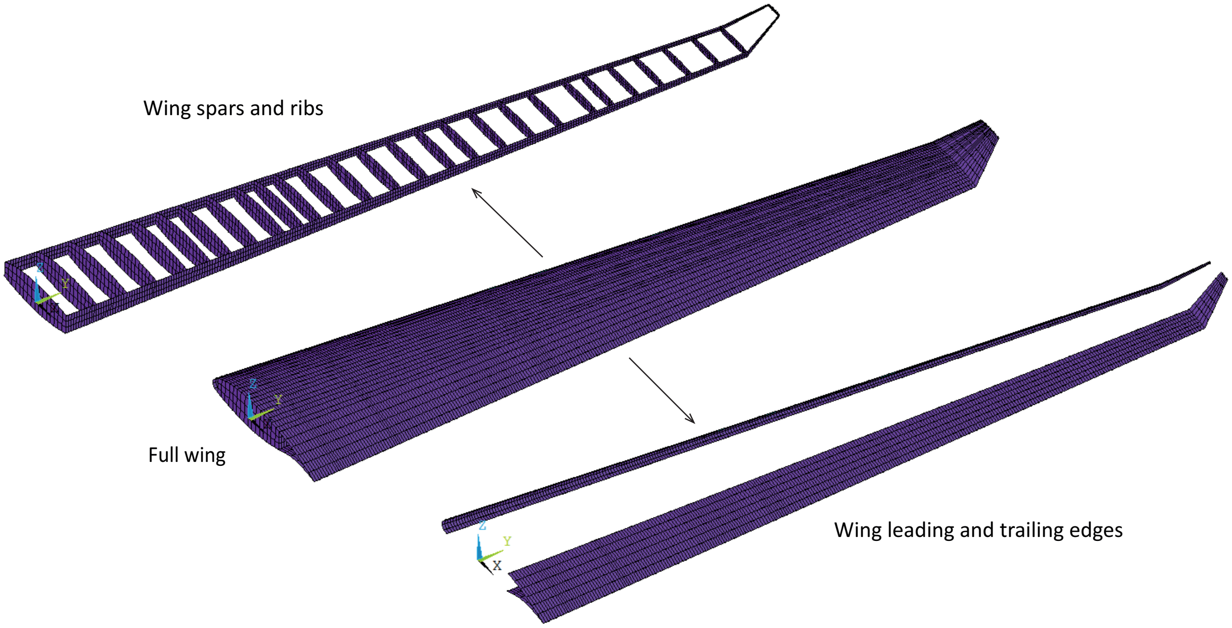

Fig. 14 An example of a wing shell FEM generated using ANSYS Mechanical APDL (*Configuration 1*).

Fig. 15 shows the mass differences of the four wing configurations relative to the baseline wing. Here, the total wing mass estimated in ANSYS includes not only the mass of skins, spars, stringers (m_{s3}), and ribs (m_{ribs}), but also that of the leading and trailing edges. It is important to note that the mass of the leading and trailing edges depends on the predefined constant thickness and the spanwise location of spars. In the current study, the thickness of the leading and trailing edges is varied between 2 mm and 6 mm to account for their contribution to the total wing mass. Note that the total mass of the baseline wing also changes with variations in the thickness of the leading and trailing edges.

As shown in Fig. 15, with increasing thickness of the leading and trailing edges, the wing mass difference δ decreases for the wide-wingbox *Configurations 1 and 2*, but increases for the narrow-wingbox *Configurations 3 and 4*. Following this trend, wide-wingbox and narrow-wingbox configurations can exhibit similar total wing mass at a specific mass contribution from the leading and trailing edges. According to the current results, a thickness of 4 mm for the leading and trailing edges yields a similar total wing mass regardless of the spanwise location of spars in the 2-spar configurations. The same behavior is expected for the 3-spar configurations when the thickness of the leading and trailing edges is increased to approximately 4.2 mm, as indicated by the intersection point of the red lines in Fig. 15.

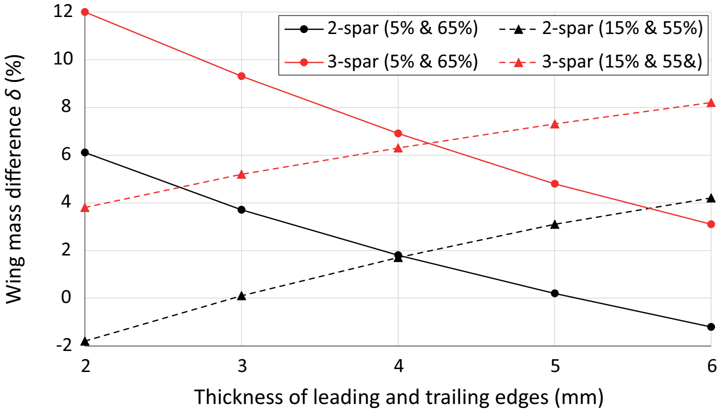

Fig. 15 Mass differences of four wings sized with different spar configurations, relative to the baseline wing that includes leading and trailing edges with corresponding thicknesses.

Further, based on this wing mass variation trend, it appears feasible to design a wide-wingbox configuration (i.e., *Configuration 1*) that is even lighter than a narrow-wingbox configuration (i.e., *Configuration 3*). On the other hand, the available wingbox volume of the wide-wingbox *Configuration 1* is approximately 39% larger than that of the narrow-wingbox *Configuration 3*, which offers significant potential for integrating a large number of batteries into the wingbox. Additionally, it is clear that the 3-spar configurations are heavier than the 2-spar configurations in both the wide and narrow wingbox cases.

Table 8 lists the maximum out-of-plane deflections, calculated by ANSYS and PROTEUS, for four wing configurations under different load cases. The average absolute difference in deflection across all cases is about 0.03 m. However, when expressed as percentages, these differences can appear relatively large when the deflections themselves are small (e.g., approximately 22% for *Configuration 4* under *Load Case 6*). The relatively small differences between the ANSYS and PROTEUS results verify the accuracy of the structural analysis solver implemented in PROTEUS.

Table 8 Comparison of maximum out-of-plane deflections (in meters), calculated by ANSYS and PROTEUS, for four wing configurations under different load cases.

Configuration		*1*	*2*	*3*	*4*
Load Case 1	PROTEUS	0.80	0.78	0.84	0.83
	ANSYS	0.83	0.82	0.90	0.90
	PROTEUS vs. ANSYS	-3.6%	-4.9%	-6.7%	-7.8%
Load Case 2	PROTEUS	2.04	1.98	2.09	2.05
	ANSYS	2.01	1.99	2.12	2.09
	PROTEUS vs. ANSYS	1.5%	-0.5%	-1.4%	-1.9%
Load Case 3	PROTEUS	-1.26	-1.23	-1.36	-1.33
	ANSYS	-1.21	-1.18	-1.32	-1.29
	PROTEUS vs. ANSYS	4.1%	4.2%	3.0%	3.1%
Load Case 4	PROTEUS	2.35	2.28	2.48	2.45
	ANSYS	2.30	2.27	2.49	2.46
	PROTEUS vs. ANSYS	2.2%	0.4%	-0.4%	-0.4%
Load Case 5	PROTEUS	1.16	1.12	1.22	1.21
	ANSYS	1.17	1.16	1.27	1.26
	PROTEUS vs. ANSYS	-0.9%	-3.4%	-3.9%	-4.0%
Load Case 6	PROTEUS	0.28	0.26	0.27	0.26
	ANSYS	0.31	0.30	0.33	0.33
	PROTEUS vs. ANSYS	-9.7%	-13.3%	-18.2%	-21.2%

VI. Conclusions

In this work, a study on the structural design and sizing of large battery-electric aircraft wings was conducted. The baseline design of the Elysian E9X aircraft wing was defined, and the critical load cases for wing sizing were identified. Wing structural sizing was performed using an in-house aeroelastic optimization tool, which aims to minimize wing mass by optimizing the thickness of wing design sections, subject to various aerostructural design constraints. Additionally, sensitivity studies on wing mass with respect to key design parameters were conducted to understand the effects of structural design and battery integration on wing mass.

According to the aircraft's V-n diagram, the maximum Pratt gust load factor at sea level is 2.37, which is slightly below the maximum manoeuvre load factor of 2.5. This indicates that the gust loads may not govern the sizing of the wing structure. Nevertheless, an equivalent gust load case (with the maximum load factor of 2.5 at sea level) is included in wing structural sizing for a conservative wing design.

Regarding the study of battery location, the results show that placing the batteries in the fuselage results in a 32% increase in wing structural mass compared to integrating them into the wing, even before accounting for the snowball effect of resizing the fuselage. For the changes in MLG spanwise location, an optimal position can be identified for minimizing wing mass. However, the influence of the MLG's spanwise location on wing mass is relatively small (within ±1%) when it is placed relatively inboard. It is important to note that this analysis considers only the landing load and does not account for taxi bump loads, which may be critical in some cases depending on the shock absorber design.

In the study of material properties, the use of high-strength aluminum alloys (e.g., 7075-T6) results in only a small mass reduction (less than 1%). In contrast, a significant wing mass reduction of approximately 22% is achieved using composite materials. However, this represents a maximum theoretical value that requires correction through further studies on layup retrieval. Additionally, increasing the thickness-to-chord ratio of both the wing root and tip airfoils can reduce the total wing mass, although the root thickness-to-chord ratio has a larger impact. A maximum reduction of approximately 8% in total wing mass can be achieved by increasing the root thickness-to-chord ratio to 25%.

The study results of four wings with different spar configurations demonstrate that, at a specific mass contribution from the wing leading and trailing edges, the wide-wingbox configuration can achieve a lower total wing mass than the narrow-wingbox configuration (e.g., 5% & 65% vs. 15% & 55%), while offering approximately 39% more available wingbox volume, which provides significant potential for integrating batteries into the wing.

Acknowledgments

This research is funded by Elysian Aircraft Company BV.

References

[1] Epstein, A. H., and O'Flarity, S. M., "Considerations for Reducing Aviation's CO_2 with Aircraft Electric Propulsion," *Journal of Propulsion and Power*, Vol. 35, No. 3, 2019, pp. 572–582.

[2] Staack, I., Sobron, A., and Krus, P., "The potential of full-electric aircraft for civil transportation: from the Breguet range equation to operational aspects," *CEAS Aeronautical Journal*, Vol. 12, No. 4, 2021, pp. 803–819.

[3] Mukhopadhaya, J., and Graver, B., "Performance analysis of regional electric aircraft," *International Council of Clean Transportation (ICCT) white paper*, 2022.

[4] Wolleswinkel, R. E., de Vries, R., Hoogreef, M. F. M., and Vos, R., "A New Perspective on Battery-Electric Aviation, Part I: Reassessment of Achievable Range," *AIAA SCITECH 2024 Forum*, 2024, p. 1489.

[5] de Vries, R., Wolleswinkel, R. E., Hoogreef, M. F. M., and Vos, R., "A New Perspective on Battery-Electric Aviation, Part II: Conceptual Design of a 90-Seater," *AIAA SCITECH 2024 Forum*, 2024, p. 1490.

[6] Werter, N. P. M., and De Breuker, R., "A novel dynamic aeroelastic framework for aeroelastic tailoring and structural optimisation," *Composite Structures*, Vol. 158, 2016, pp. 369–386.

[7] Rajpal, D., Kassapoglou, C., and De Breuker, R., "Aeroelastic optimization of composite wings including fatigue loading requirements," *Composite Structures*, Vol. 227, 2019, p. 111248.

[8] Wang, Z., Peeters, D., and De Breuker, R., "An aeroelastic optimisation framework for manufacturable variable stiffness composite wings including critical gust loads," *Structural and Multidisciplinary Optimization*, Vol. 65, No. 10, 2022, p. 290.

[9] Krüger, W. R., Meddaikar, Y. M., Dillinger, J. K. S., Sodja, J., and De Breuker, R., "Application of aeroelastic tailoring for load alleviation on a flying demonstrator wing," *Aerospace*, Vol. 9, No. 10, 2022, p. 535.

[10] Wang, Z., Liu Xu, V. Q., and De Breuker, R., "Preliminary aeroelastic optimization of electric aircraft wings including propeller whirl flutter effects," *Aerospace Science and Technology*, Vol. 157, 2025, p. 109813.

[11] Ferede, E., and Abdalla, M., "Cross-sectional modelling of thin-walled composite beams," *55th AIAA/ASMe/ASCE/AHS/SC Structures, Structural Dynamics, and Materials Conference*, 2014, p. 0163.

[12] Werter, N. P., De Breuker, R., and Abdalla, M. M., "Continuous-time state-space unsteady aerodynamic modeling for efficient loads analysis," *AIAA Journal*, Vol. 56, No. 3, 2018, pp. 905–916.

[13] Svanberg, K., "A class of globally convergent optimization methods based on conservative convex separable approximations," *SIAM Journal on Optimization*, Vol. 12, No. 2, 2002, pp. 555–573.

[14] Rajpal, D., Gillebaart, E., and De Breuker, R., "Preliminary aeroelastic design of composite wings subjected to critical gust loads," *Aerospace Science and Technology*, Vol. 85, 2019, pp. 96–112.

[15] Sodja, J., Werter, N. P. M., and De Breuker, R., “Aeroelastic Demonstrator Wing Design for Maneuver Load Alleviation Under Cruise Shape Constraint,” *Journal of Aircraft*, 2021, pp. 1–19.

[16] EASA, “Certification specifications and acceptable means of compliance for large aeroplanes CS-25,” *Amendment*, Vol. 25, 2023.

[17] Pratt, K. G., and Walker, W. G., “A revised gust-load formula and a re-evaluation of V-G data taken on civil transport airplanes from 1933 to 1950,” Tech. rep., 1954.

[18] Ardema, M. D., Chambers, M. C., Patron, A. P., Hahn, A. S., Miura, H., and Moore, M. D., “Analytical Fuselage and Wing Weight Estimation of Transport Aircraft,” Tech. rep., NASA-TM-110392, 1996.

[19] Kassapoglou, C., *Design and Analysis of Composite Structures: With Applications to Aerospace Structures*, John Wiley & Sons, Ltd, 2013.

[20] Macquart, T., “OPTIBLESS: An open-source toolbox for the optimisation of blended stacking sequence,” *17th European Conference on Composite Materials 2016*, European Conference on Composite Materials, ECCM, 2016.